An Electrostatic Zigzag Transmissive Microoptical Switch for MEMS Displays

Kerwin Wang, Michael Sinclair, Gary K. Starkweather, and Karl F. Böhringer, *Senior Member, IEEE*

***Abstract*—This paper presents the design and characterization of the zigzag transmissive microoptical switch. It consists of a highly space-efficient zigzag electrostatic actuator and opaque shutter pair, which cover the optical channel in order to modulate a focused incident light beam. The novel zigzag design increases the electrostatic force and extends the stable travel range of the electrostatic actuator. By adjusting the dimensions of the zigzag, it can operate both under digital and analog optical switching. The real-time shutter motions have been tested by a laser-integrated microscope. Experimental data demonstrate that a zigzag electrostatic actuator of $47\ \mu\mathrm{m} \times 160\ \mu\mathrm{m}$ size can achieve a maximum static lateral displacement of 10 μm (18 μm total opening by a shutter pair) at 38 V. Depending on their design, zigzag devices have a mechanical resonance frequency of up to 38.6 kHz with response time less than 20 μs and lifetime above 7.6×10^9 cycles. [1661]**

***Index Terms*—Electrostatic actuator, micro-optics, microopto-electromechanical system (MOEMS), optical switch, transmission display.**

I. Introduction

TRANSMISSIVE microoptical switches (TMOS) have played a critical role in optical telecommunication systems, optical network security systems, and also the James Webb space telescope [2]. In general, TMOS have a highly tunable optical output power range between on and off states that makes transmissive technology one of the most promising candidates to realize a high-contrast, self-illuminating pixel display. In principle, a TMOS display can yield brighter and sharper images than most of the existing displays [3]–[12]. However, TMOS display technology has remained underdeveloped because it is difficult to design a free space, cost effective, sufficiently fast and power efficient actuator that fits into a self-illuminated display pixel (e.g., a 125-μm-squared area). Developing a novel actuator design to simultaneously achieve all these design goals under the various constraints imposed by material limits and process resolution of a commercially available MEMS process (e.g., MEMSCAP MUMPs) is even more challenging.

This paper introduces the zigzag electrostatic actuator for TMOS (see Fig. 1). The novel zigzag structure improves the force-to-stiffness ratio of conventional electrostatic actuators. Because the actuators cannot share their working space with the light path without blocking the light, the TMOS design incorporates microlens arrays to form a complete display module that improves the optical efficiency and space coverage. Each microlens focuses its portion of the light into a tunnel under the optical shutter; the shutter can modulate the light passing through the aperture depending on its opening dimensions. Another microlens array behind the TMOS array projects the light onto a display screen or display module (see Fig. 2).

To initiate the TMOS design process for a practical display, we first discuss in Section II the design constraints given by the naked human eye. The eye's acuity and response information can be useful for determining TMOS size and speed. Then, we present an approach to determine the minimal size of the optical tunnel opening; it is constrained by the diffraction limit of light and by microlens properties. In Section III, we review state-of-the-art electrostatic actuation technologies and introduce the zigzag actuator to achieve the design goals discussed in the previous section. We develop a flexibility model from the virtual work principle for zigzag structures. This model is used to estimate the fundamental resonance frequency of the zigzag structure by Dunkerley's method. We discuss the fringe effect in detail by comparing the electrostatic forces estimated with an analytic approach and with an electric field simulator. As a consequence, a zigzag width-frequency design space is established. Fringing can be useful in actuator design to increase the electrostatic force-to-stiffness ratio; practical implications are demonstrated in physical devices. Then, in Section IV, we describe a DRIE-based postprocess on the backside of a 1 cm^2 polysilicon MUMPs chip for the optical tunnel etching underneath the shutters. The post-process ends with a PECVD hydrophobic fluorocarbon polymer coating for good electrical isolation and low in-use stiction. In Section V, we present time-resolved testing results. They show that depending on their geometry, zigzag actuators can be driven under both digital and analog switching modes. Under analog mode, the shutter can have full range controllable motion without pull-in. All the design goals are achieved.

Manuscript received July 23, 2005; revised May 31, 2006. This work was supported in part by a gift from Microsoft Research. The authors gratefully acknowledge equipment and software donations from Agilent Technologies, Intel Corporation, Tanner Research, Inc. and Technic, Inc. The work of K. F. Böhringer was supported in part by an NSF CAREER award and by an Invitational Fellowship for Research in Japan from the Japan Society for the Promotion of Science (JSPS). This paper extends on a prior conference publication at the *12th International Conference on Solid-State Sensors and Actuators (Transducers'03)* Boston, MA, June 6–12, 2003 [1]. Subject Editor O. Solgaard.

K. Wang and K. F. Böhringer are with the Department of Electrical Engineering, University of Washington, Seattle, WA 98195-2500 USA (e-mail: kww@u.washington.edu).

M. Sinclair and G. K. Starkweather are with Microsoft Research, Redmond, WA 98052 USA.

Color versions of one or more of the figures in this paper are available online at http://ieeexplore.ieee.org.

Digital Object Identifier 10.1109/JMEMS.2006.888913

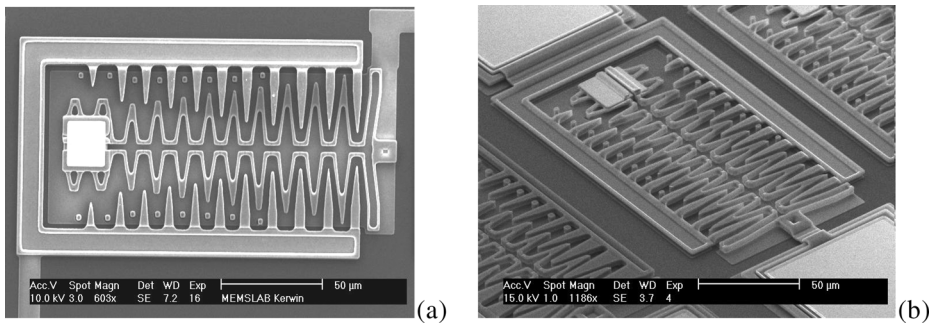

Fig. 1. SEM micrographs of zigzag actuator pair (a) top view. (b) Perspective view.

II. Design of the Transmissive Optical Switch

The TMOS consists of actuators, shutters and a miniaturized optical tunnel (see Fig. 2). Here we list the crucial design constraints and goals for making a sequence of design decisions:

1) Determination of device size by checking the human eye's acuity and resolution angle from a comfortable viewing distance for proper image pixel size and resolution.
2) Checking the limitation of working frequency (switching speed) by examining the eye's critical flicker frequency for stable imaging.
3) Determination of geometry of the optical tunnel and the shutter opening size by calculating the diffraction limit, depth of focus and numerical aperture (NA) with a coupled microlens for good transmissive light efficiency.
4) Creating a novel TMOS device by dual shutter and zigzag electrostatic actuator design for high speed, space-efficient, low voltage transmissive micro-optical switching.

The first three decisions are briefly summarized below; the shutter and actuator design is discussed in detail in Section III.

A. TMOS Size and Resolution

For now let us assume that each TMOS represents one screen pixel on a single-color flat-panel display. The size of the physical TMOS device should be equal to or less than the screen pixel size, which is limited by the comfortable viewing distance due to the eye's acuity. Most people can distinguish one resolution angle feature ($1 \text{ resolution angle} = 1 \text{ arc min} = 1/60°$). For example, when looking at a computer monitor, the distance between eyes and screen is around 45 cm. Then, the minimal distinguishable feature size for 1 arc minute is equal to $45 \text{ cm} \times \sin(1') = 130.9\ \mu\text{m}$. Choosing the TMOS pitch (equal to microlens pitch and pixel size) of 125 μm satisfies this acuity constraint and conforms to the resolution standards for displays to obtain an HDTV quality image on an 11-inch or larger monitor.

B. Working Frequency

The main constraints on the working frequency of a TMOS are imposed by the display frame rate and a human eye's critical flicker frequency. Under analog mode, the TMOS shutter opening directly controls the brightness of a pixel. In this case, to see a stable image, the shutter speed should be greater than 60 Hz for flicker-free operation. Alternately, under digital mode, control of pixel brightness is achieved by varying the duty cycle of the shutter. To control the pixel brightness at a rate of 60 frames/s, an 8-bit, 256-level gray scale (monochrome) pixel should be implemented by a TMOS at the working frequency of 15.36 kHz ($= 60 \text{ Hz} \times 256$). Thus, 15.36 kHz is chosen as the design goal for our TMOS operation.

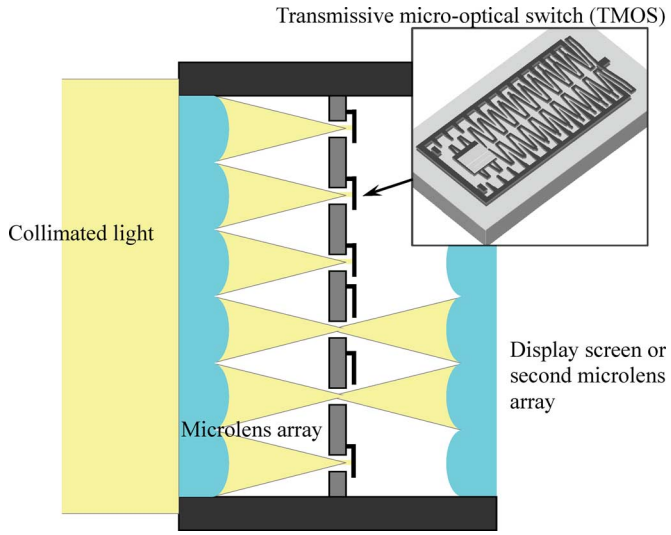

Fig. 2. Cross-sectional view of an integrated TMOS display: From left to right, the collimated light is focused by a microlens array, passes through an optical tunnel, is attenuated by the TMOS and projected to a display screen or a second collimating microlens array; upper right: conceptual perspective view of zigzag TMOS.

C. Optical Tunnel Design

An optical tunnel allows light focused by various microlens systems to transmit through the substrate and reach the shutters (Fig. 2). From the aspects of actuator design and scaling effects, a small tunnel implies a small actuator size, small displacement, low driving voltage, low power consumption, and higher operating frequencies. Thus, a small tunnel under the shutter is preferred. However, the hole cannot shrink to zero size because of the limitations on diffraction spot size, numerical aperture, and depth of focus (see Fig. 3).

1) Diffraction spot size $DS = 2.44\lambda(f/D)$ [13], where λ is wavelength, D is aperture, f is the focal length and f/D is the focal number or focal ratio of the lens. Thus we obtain the constraint $w \geq 2.44\lambda_{\max}(f/D)$, where $\lambda_{\max}$ is the largest wavelength in use.

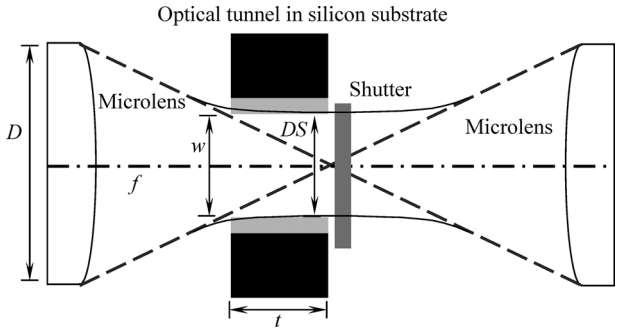

Fig. 3. Diffraction spot size DS, numerical aperture $NA = D/(2f)$, and depth of focus $\mathrm{DOF} > t$ in a TMOS, resulting in geometric constraints on the optical tunnel width w and substrate thickness t.

2) Microlens numerical aperture (NA), which is defined as $NA = D/(2f)$. The diameter and depth of the tunnel limits the selection of the numerical aperture of the lens system. Given the diameter of the cylindrical tunnel w and the substrate thickness t (Fig. 3), the geometry of the optical path requires $w/t > D/f$. Assuming $w = DS$ and incorporating the diffraction spot size defined in the first limitation above, we get $t < 2.44\lambda_{\max}(f/D)^2 = 0.61\lambda_{\max}/NA^2$.
3) Depth of focus (DOF) is defined as the range from the focal plane over which the working beam diameter varies within a specified limit. Depending on irradiance conditions and requirements, DOF can be represented in different formats [13]. In our case, when using a diffraction-limited microlens system $(\mathrm{Fresnel\ number} > 5)$, the substrate thickness t should be smaller than DOF, thus $t < 2\lambda_{\min}(f/D)^2 = \lambda_{\min}/2NA^2$, otherwise a significant fraction of light would be blocked at the tunnel boundaries (see again Fig. 3). $\lambda_{\min}$ is the shortest wavelength in use.

Combining above constraints and choosing a diffraction-limited lens system with $8 < f/D < 20$ (these values are commonly available in microlens systems), $\lambda_{\min} = 420$ nm and $\lambda_{\max} = 760$ nm for visible wavelengths, we obtain the feasible design space. Note that constraint 3 always dominates constraint 2; however, when using a large range of wavelengths $[\lambda_{\min}, \lambda_{\max}]$, constraint 1 imposes a larger value on w than needed for $\lambda_{\min}$; therefore, in practice we can relax constraint 3 and only enforce constraint 2. For smaller f-number, aberrations have an adverse effect on both the spot size and depth of focus, whereas if the solution space is above f/8, aberrations are negligible.

The design space in Fig. 4 shows that $w = 14.8\ \mu$m is the minimal allowed diameter for the optical tunnel. However, a conservative design strategy, using a larger cylindrical opening w and smaller substrate thickness t, would avoid optical loss in the optical tunnel by tolerating misalignment or process-induced lens quality variation. A thinner substrate fits both low and high NA lens systems; the major limitation on substrate thickness is its mechanical strength. For example, if $f/D = 10$, then DS is around 18.5 μm. Therefore, a 20-μm tunnel diameter is set up as a design goal, a substrate thickness of 150 μm is chosen for good optical transmission and mechanical strength.

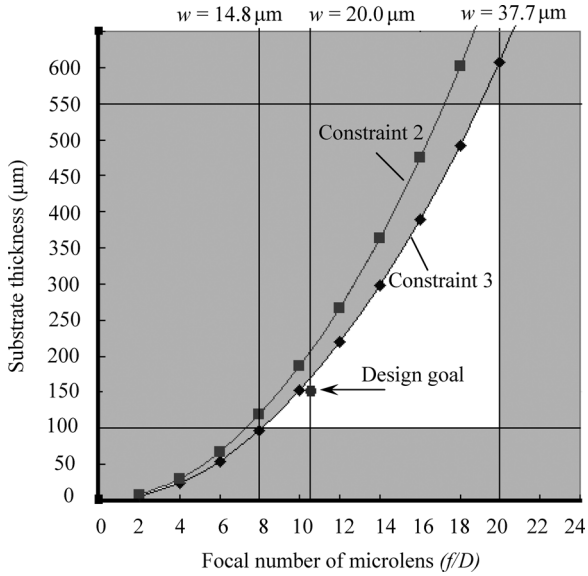

Fig. 4. Design space of TMOS for visible light of wavelength $\lambda = 760$ nm. The white region shows the feasible range for f/D and t. The region is bounded from below by minimum substrate thickness, from left and right by minimum and maximum focal number f/D, and from above by diffraction spot size DS (constraint 2) and depth of focus DOF (constraint 3).

TABLE I
DESIGN PARAMETERS AND GOALS FOR THE TRANSMISSIVE OPTIC SWITCH

Parameters and goals	Value
Device pitch	125μm in *x* and *y* direction
Working frequency	15.36kHz
Tunnel size	20μm inner diameter
Substrate thickness	150μm
Feasible *f/D* system	10
Lens aperture *D*	125μm
Focus	*f*=1.25mm

A $30 \times 30\ \mu\mathrm{m}^2$ shutter is sufficient to block the light emanating from this spot. Misalignment between center of the shutters and the tunnel should be controlled within submicron range. As a summary, all the critical dimensions are put together in Table I.

Because no existing microactuator could achieve all these design goals, we have developed a novel electrostatic zigzag design. A brief review of electrostatic actuator designs is given in the next section and corresponding state-of-the-art examples are described before the zigzag electrostatic actuator driven TMOS design is detailed and corresponding analytical studies are given.

III. ELECTROSTATIC ZIGZAG ACTUATOR AND OPTICAL SHUTTER DESIGN

Electrostatic microsensors and microactuators have been widely used in MEMS for more than two decades [14], [15] because of their low energy consumption, good scaling properties to small dimensions and high energy densities. They can be roughly classified into two categories, parallel-plate drives and comb drives.

Parallel-plate drives have an electrostatic field inside the gap parallel to the electrode movement direction with a nonlinear relationship between electrostatic force and displacement. The

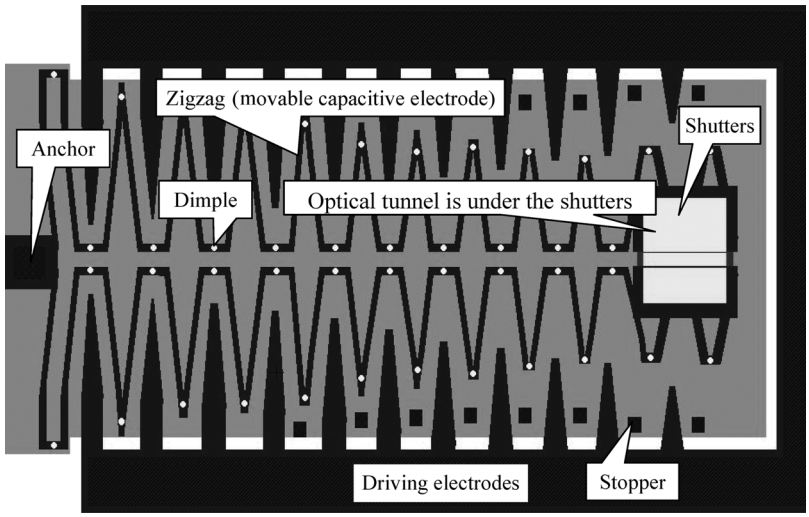

Fig. 5. CAD layout diagram of the zigzag actuator design for a TMOS.

stable travel of parallel-plate electrostatic actuators is restricted to one third of the initial gap size due to pull-in behavior [16]. Several methods have been proposed to extend the usable range of parallel-plate drives, involving closed-loop voltage control [17], series capacitance [18], [19], leveraged bending [20] and curved electrodes or structures [21], [22]. Series feedback capacitors can rapidly increase in capacitance when the movable electrode goes beyond one-third of the original gap to provide the negative feedback to stabilize the actuator. A closed-loop controller requires a complicated feedback sensing and control system. Leveraged bending also needs more device area for anchors and the increased range of motion.

Comb drives [23]–[28] have an electrostatic field inside the gap perpendicular to the electrode motion direction. Traditional linear comb drive designs showed limited force output and forward displacement due to electromechanical side instability when electrostatic side forces, orthogonal to the comb teeth, overwhelm the suspension stiffness. Various comb shapes and configurations of electrodes have been studied to maximize force generation capability and customize stable force-displacement response for a variety of applications including a submicron gap comb-drive [29], an angled comb finger design [30] and shaped-finger comb drives [31]–[33]. Furthermore, several suspension designs, including crab-leg flexures [34], clamped-clamped beams [35], and folded beam suspensions [36] have been shown to improve the travel range and stability. Overall, comb drives take up a large area for combs and long suspending springs to provide high force-to-stiffness ratios for larger displacements.

A. Zigzag Actuator Design

All these designs of moving parts, electrodes and suspensions of electrostatic actuators, including both parallel-plate drives and comb drives, have been attempted to increase the driving force, traveling distance, or stability. However, these designs are still too large to fit into a TMOS. There are two fundamental approaches to improve the force-to-stiffness ratio and space efficiency of electrostatic designs for TMOS. One takes advantage of the scaling effect to make densely arranged combs and narrowly fabricated suspensions. The other one exploits novel actuator designs and architectures.

This paper avoids downscaling below typical MEMS dimensions and related difficulties associated with the first approach; instead it takes the second approach and proposes the zigzag electrostatic actuator. The unique design combines a flexible zigzag suspension and angled finger-shaped combs into a single integrated structure. Fig. 5 shows the schematic diagram of the zigzag drive design for the TMOS. Each zigzag in the TMOS can take care of half of the required motion for the opening. In its rest position, the movable zigzag teeth (capacitive electrodes) and stationary angled electrodes are partially engaged. The sizes of the teeth gradually decrease towards the free ends to allow a larger range for the shutter movement. The mechanical restoring force of the zigzag keeps the shutter idle at the closed position. When the zigzags are activated by a voltage, the shutters open symmetrically to opposite sides of the optical channel. Each zigzag drive has linear disengaging teeth (teeth are getting smaller and the gap is getting larger at a linear rate) and a relatively long suspension and range of motion of the shutters. The teeth with their folded flexure work both like an extended flexible spring and a shape-modified comb. They can make very efficient use of the available space by simultaneously increasing the driving force and decreasing the spring stiffness and achieve significant stable displacement within limited space and driving voltage.

The zigzag suspensions have dimples to reduce in-use sticking. The use of mechanical stoppers to define the open shutter position may increase positional accuracy and switching speed under digital operation mode. It allows pull-in to yield a consistent shutter opening. Stoppers set along the electrodes also can prevent short-circuits and diminish the risk of failure. A ground plate is located under the movable zigzag, which is connected to the same potential as the movable structures via anchors to prevent electrostatic pull-down forces to the substrate.

The shutters are made from an opaque cover layer over the optical channel, in order to modulate an incident light beam. Ideally, most of the light focused by the microlens passes through

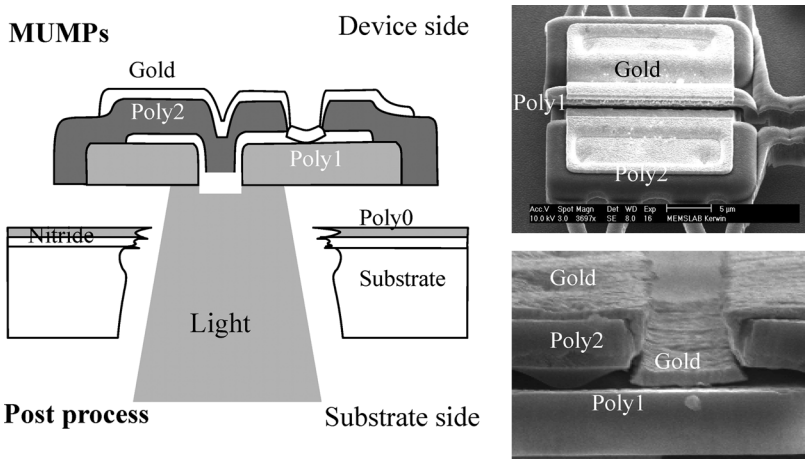

Fig. 6. Schematic cross section (left) and SEM micrograph (right) of optical shutter design. An opaque gold layer covers the polysilicon microshutters.

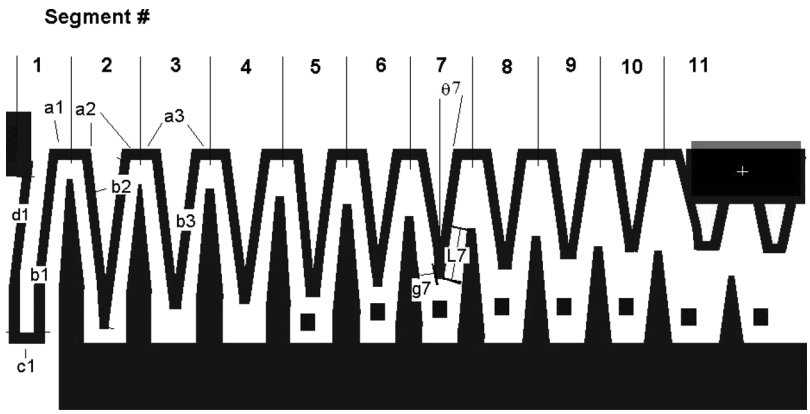

Fig. 7. Detailed CAD layout of a typical zigzag design with geometric parameters.

the optical tunnel, and couples to another collimating microlens. The masses of both shutters in a TMOS are equal to achieve a balanced resonance frequency and stable dynamic performance of the shutter pair (Fig. 6). All of the TMOS components (shutters, zigzags, electrodes, stoppers, and anchors) can be arranged into a compact rectangle.

To capture the physical characteristics and the trends in device performance in response to design variations, the next subsection presents a parametric study on stiffness, natural frequency and electrostatic force of a zigzag drive by analytical approximation.

B. Design Analysis

A sketch of a zigzag actuator with its design parameters is shown in Fig. 7 and Table II. To produce full gap movement of the shutter while maintaining a reasonable voltage, the stiffness and electrostatic force of the zigzag are critical. While these properties are tunable by the zigzag geometry, their precise relationship is quite complicated.

1) Stiffness Model: Several assumptions can be made to simplify the flexibility analysis of the zigzag structure in its switching (latitudinal) direction:

1) the shutter deflection is caused by zigzag bending only (no stretching or twisting); its connection to the folded zigzag is rigid;

TABLE II
DESIGN PARAMETERS FOR THE ZIGZAG ACTUATOR IN FIG. 7

i	a_i	b_i	c_1	d_1	θ_i	L_i (μm)	$L_{i,l}$ (μm)	$L_{i,r}$ (μm)	$g_{i,l}$ (μm)	$g_{i,r}$ (μm)
1	3	41	6	32	7.5	-	-	-	-	-
2	3	38	-	-	7.5	32	30	29	2.4	2.2
3	3	34	-	-	7.5	30	25	24	2.4	2.3
4	3	32	-	-	8.3	25	23	22	2.4	2.4
5	3	30	-	-	8.4	23	21	19	2.4	2.4
6	3	29	-	-	8.6	20	17	14	2.6	2.5
7	3	27	-	-	8.7	15	13	10	2.9	2.6
8	3	26	-	-	9.0	12	12	8	3.1	3.0
9	3	24	-	-	9.3	7.8	9	7	4.4	3.3
10	3	22	-	-	9.8	3.5	5	3	5.7	3.5

2) the zigzag has a linearly elastic structure within the range of maximum deflection.

The zigzag, which consists of differently sized segments, is anchored at the first suspension (b_1, c_1, d_1). Each segment consists of four connected angled trusses (e.g., a_2, b_2, b_2, a_2). They represent one "tooth" of the zigzag. By integrating the flexibility at each segment, from the unit load method [37] one can obtain the flexibility of the entire zigzag. Let M_u be the bending moment caused by the displacement Δ corresponding to a unit load. With the above assumptions, only M_u needs to be considered when calculating the virtual work, and we can obtain the

general equation for displacement in response to a unit load in the following form [37]:

$$\Delta = \int \frac{M_u M_L dx}{EI}. \tag{1}$$

M_L represents the bending moment caused by the actual load. E and I represent the modulus of elasticity and area moment of inertia, respectively. To find the flexibility B of a given structure, we replace the actual applied bending moment M_L with the unit bending moment M_u in (1), and the flexibility of the zigzag structure can be represented as

$$B = \int \frac{M_u^2 dx}{EI}. \tag{2}$$

B, the flexibility, is measured in m/N. Based on (2) the flexibility of the zigzag structure in Fig. 7 can be integrated according to the following equation (3). Assuming the zigzag has uniform width and moment of inertia everywhere, we find the flexibility B_n at the right end of segment n when a unit load is applied

$$\begin{aligned} B_n = \frac{1}{EI}\Bigg(& \int_0^{d_1} (L_{n,1} + x\sin\theta_1)^2 dx \\ & + \int_0^{c_1} (L_{n,1} + d_1\sin\theta_1 - x)^2 dx \\ & + \int_0^{b_1} (L_{n,1} + d_1\sin\theta_1 - c_1 - x\sin\theta_1)^2 dx \\ & + \int_0^{a_1} (L_{n,1} + (d_1 - b_1)\sin\theta_1 - c_1 - x)^2 dx \\ & + \int_0^{a_2} (L_{n,2} - x)^2 dx + \int_0^{b_2} (L_{n,2} - a_2 - x\sin\theta_2)^2 dx \\ & + \int_0^{b_2} (L_{n,2} - a_2 - b_2\sin\theta_2 - x\sin\theta_2)^2 dx \\ & + \int_0^{a_2} (L_{n,2} - a_2 - 2b_2\sin\theta_2 - x)^2 dx + \cdots \\ & + \int_0^{a_n} (L_{n,n} - x)^2 dx + \int_0^{b_n} (L_{n,n} - a_n - x\sin\theta_n)^2 dx \\ & + \int_0^{b_n} (L_{n,n} - a_n - b_n\sin\theta_n - x\sin\theta_n)^2 dx \\ & + \int_0^{a_n} (L_{n,n} - a_n - 2b_n\sin\theta_n - x)^2 dx \Bigg). \end{aligned} \tag{3}$$

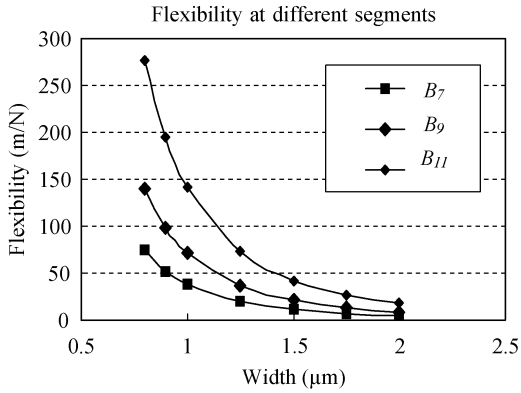

Fig. 8. Graph relating the stiffness of zigzag segments to their widths, calculated with the unit load method.

E	Young's modulus.
$I = (tw^3)/12$	Area moment of inertia.
B_n	Flexibility at segment n.
$L_{n,i}$	Effective length for calculating bending moment at the left edge of segment i when unit load is applied to the right edge of segment n; e.g., $L_{1,1} = 0$ and $L_{2,1} = (d_1 - b_1)\sin\theta_1 - c_1 - a_1$.
a_i, b_i, c_i, d_i	Length of beams a, b, c, d at segment i, and θ_i the corresponding beam skew angle.
w, t	Beam width and thickness.
x	The local coordinate along each beam segment.

Subscript i refers to the segments a_i, b_i, c_i, and d_i of the zigzag in Fig. 7. The zigzag flexibility at the end of each segment is a combination of the flexibility at the individual segment and the flexibility of the entire suspension to its left.

A simple way to modify the flexibility is to adjust the width of the individual angled teeth. The parametric designs of zigzags and electrodes have been described in Table II. A graph comparing the stiffness of zigzag segments with a variety of widths is shown in Fig. 8. The flexibility information at each segment of the zigzag can help predict the fundamental resonance frequency of the zigzag.

2) Natural Frequency: By using the flexibility and mass information of each zigzag segment and shutter, one can estimate the fundamental resonance frequency of the zigzag actuator from Dunkerley's method [38]. The method yields the following expression to estimate a lower bound of fundamental resonance frequency

$$\begin{aligned} & \frac{1}{\omega_1^2} + \frac{1}{\omega_2^2} + \ldots + \frac{1}{\omega_n^2} \\ & \quad = (B_1 m_1 + B_2 m_2 + \ldots + B_n m_n) \\ & \quad \Rightarrow \frac{1}{\omega_1^2} < (B_1 m_1 + B_2 m_2 + \ldots + B_n m_n) \\ & \quad \Rightarrow \omega_1 > 1/\sqrt{B_1 m_1 + B_2 m_2 + \ldots + B_n m_n}. \end{aligned} \tag{4}$$

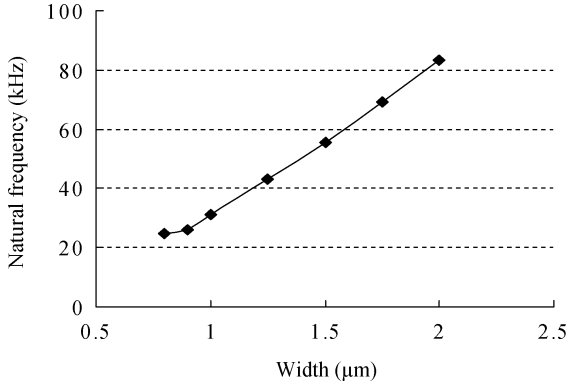

Fig. 9. Width-frequency design space for the zigzag design given in Fig. 7, calculated with the unit load method.

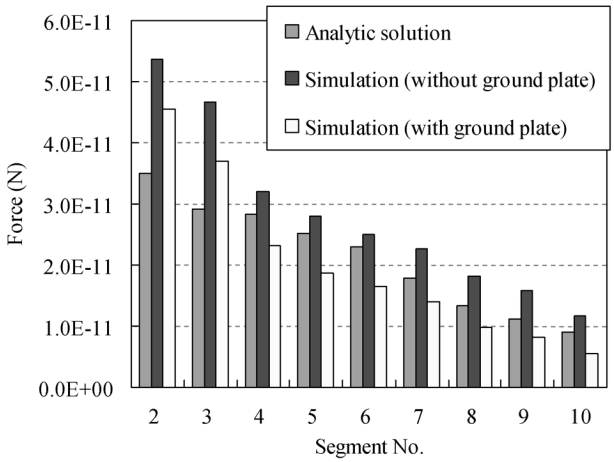

Fig. 10. Comparison between analytic method and FEM simulations for the force F_{es} along the latitudinal direction, with a voltage $V = 1\,\mathrm{V}$.

B_i is the flexibility at segment i (in m/N), m_i the mass at segment i (kg), ω_1 the fundamental resonance frequency, and $\omega_2, \omega_3, \ldots$ the higher mode resonance frequencies. Since all higher modes can be assumed to be much higher than ω_1 we can make the following approximation:

$$\omega_1 \approx 1/\sqrt{B_1 m_1 + B_2 m_2 + \ldots + B_n m_n}. \tag{5}$$

Assuming the total length of the zigzag suspension is given as a design constant, the basic geometric parameters to manipulate the zigzag natural frequency are mainly the zigzag angles θ_i and width w. Holding the zigzag angle constant, the equations for resonance frequency may be combined to form a single expression defining the width-frequency design space (see Fig. 9). These theoretically calculated frequencies have been checked against experimental results and will be discussed in Section V.

3) Electrostatic Energy and Force: The capacitance of each zigzag segment with respect to the gap between the segment and electrode is important for calculating the change in electrostatic potential energy and electrostatic force. If we neglect (for now) the fringe effect in the zigzag geometry, the electrostatic potential energy U_{es} between the movable and the stationary electrode of zigzag segment i can be derived from its capacitance and expressed as

$$U_{es} = \frac{V^2}{2}\varepsilon_0\varepsilon_r t\left(\frac{L_{i,l} + y_i\cos\theta_{i,l}}{g_{i,l} + y_i\sin\theta_{i,l}} + \frac{L_{i,r} + y_i\cos\theta_{i,r}}{g_{i,r} + y_i\sin\theta_{i,r}}\right). \tag{6}$$

Here, $L_{i,l}$ and $L_{i,r}$ represent, respectively, the effective (engagement) comb length on the left and on the right of the i^{th} segment, $g_{i,l}$ and $g_{i,r}$ are the left and right gap in the rest position, and θ_i is the beam skew angle. y_i represents the displacement of segment i in the latitudinal direction. ε_0 is the electrical permittivity of free space, ε_r the dielectric constant of the medium in the gap, and V is the electrical potential between the moving and the stationary electrode (see again Fig. 7 and Table II).

The magnitude of the electrostatic force F_{es} on a segment i depends on the applied voltage as well as the geometry of the shaped electrodes. F_{es} can be determined from the first variation of potential energy with respect to displacement, $F_{es} = dU_{es}/dx$. From this relationship, it follows that

$$F_{es} = \frac{V^2}{2}\varepsilon_0\varepsilon_r t\left(\frac{L_{i,l}\sin\theta_{i,l} + g_{i,l}\cos\theta_{i,l}}{(g_{i,l} + y_i\sin\theta_{i,l})^2} + \frac{L_{i,r}\sin\theta_{i,r} + g_{i,r}\cos\theta_{i,r}}{(g_{i,r} + y_i\sin\theta_{i,r})^2}\right). \tag{7}$$

Equation (7) implies that the zigzag actuator, unlike a comb-drive, exhibits a nonlinear force with respect to latitudinal displacement. The force F_{es} acting on the zigzag is a function of zigzag shape and gap size. Fig. 10 compares F_{es} along the latitudinal direction for each segment i, estimated by the analytic method of (7) and also by an electrostatic field simulator (see Section III-B4). The segments near the anchor experience a larger force because the apex of the zigzag is closer to the electrode. However, the segments near the shutter contribute more to torque and bending moment as they move close to the fixed electrode. Achieving a maximum stroke (i.e., shutter displacement) $y_{\max}$ within a given area is the overall design goal. The angle θ_i and the stroke (i.e., the motion range of each zigzag segment) can be identified as two major geometric design parameters.

Holding the segment lengths and voltage constant, the relationship between skew angle and force has been checked analytically for two different zigzag stroke vectors (see Figs. 11 and 12). The angle-force design space is checked for θ_i between 0 and 30 degrees. This analysis indicates that increasing zigzag skew angle increases the force generation especially for larger strokes near the shutter. In both figures, segments with lower index number have less flexibility and stroke, because they have small gaps for generating large electrostatic forces. Therefore, the generated force is less sensitive to their skew angle. For zigzag segments near the shutter, the increase in skew angle has significant impact on the driving force especially for large strokes (see Fig. 12). However, within a limited device area, the

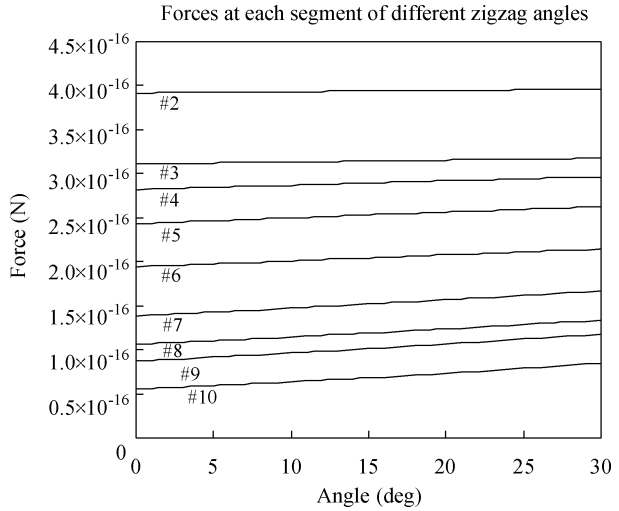

Fig. 11. Skew angles vs. electrostatic force for stroke vector [0.05 0.1 0.25 0.4 0.5 1.0 1.5 2.0 3.0] calculated with the analytical model. The stroke vector represents the stroke of each zigzag tooth from segment no. 2 to no. 10 in micrometers.

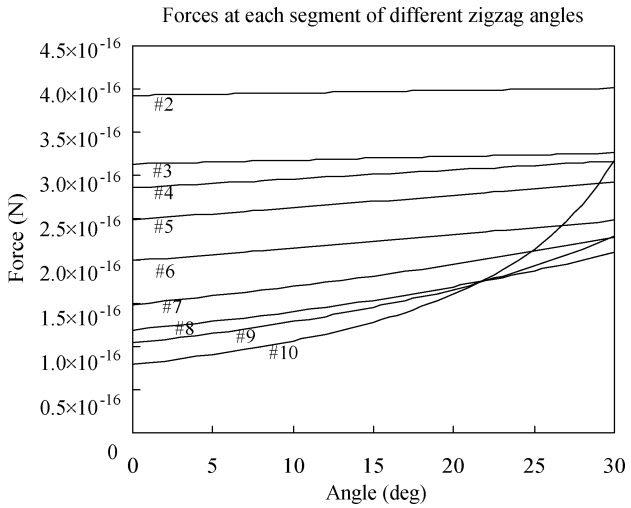

Fig. 12. Skew angles versus electrostatic force for stroke vector [0.1 0.2 0.5 0.8 1.0 2.0 3.0 4.0 6.0] calculated with the analytical model.

tradeoff is an increase in stiffness and a reduction in the amount of zigzag teeth.

In general, the design of the zigzag actuator is chosen to fulfill a given specification for high force-to-stiffness ratio and space efficiency. The simplest way to increase the maximum displacement given a limited design area is to reduce the width of an individual zigzag segment rather than modifying zigzag lengths and angles. Thus, the width of the zigzag structure will usually be chosen as the minimum feature size of the fabrication process.

4) Fringing Effects: The analytical closed-form solution of (7) does not consider the fringe effect. Thus, the calculated force of each segment has been compared with the result determined by a three-dimensional FEM electrostatic solver, the Maxwell 3-D field simulator [39]. It computes capacitance, electric field, and energy caused by dc voltages. See again Fig. 10.

Two types of three-dimensional models have been computed and compared: The first model does not take a ground plate into consideration, the second model does; the ground plate is at the same voltage as the moving zigzag structure (as in the physical device). The results show that 1) when there is no ground plate, then the fringe field is fully developed, producing the highest force output among the three estimation methods; 2) with the ground plate, the fringe field is only halfway developed, and the analytic solution can overestimate the actual electrostatic force. The overestimation happens at segments above no. 3 because there is a "charge competition" between the ground plate and the zigzag: more electrostatic energy is stored between the fixed electrode and ground plate than between zigzag segment and ground plate.

However, the fringe effect may be useful in actuator designs to increase the electrostatic force-to-stiffness ratio. Maxwell simulation results show that different thickness combinations of zigzag structures and electrodes allow us to exploit fringing effects and to reduce the driving voltage. Under the same applied voltage and gap size, the single height zigzag has more deflection than the double height structure because of the relatively higher force contribution from the fringing field. For example, when the height of the beam decreases from 3.5 to 2.0 μm, the stiffness decreases 43% but the electrostatic force decreases only 28%. Thus, under the same applied voltage and gap, the single height zigzag has more deflection than the double height structure. This insight can be exploited to improve the electrostatic force-to-stiffness ratio of the zigzag actuator.

5) Design Fine-Tuning: Ideally (under small deflection), the displacement of the zigzag during deflection would follow a straight trajectory. During actual operation, the deflection of the zigzag follows a slightly curved trajectory, especially for the movable zigzag segments near the shutter, because the increasing electrostatic field causes a slight compression of the zigzag segments. Thus, the fixed electrode near the shutter is shifted longitudinally towards the anchor by around 2 μm. Therefore, when the actuator is fully opened to the stoppers, the zigzag segment does not contact with the stationary electrode, even though a straight trajectory would result in a collision. This kind of design information for the final adjustment of zigzag electrode position is gained from the design-fabrication-testing-modification (DFTM) loop. Moreover, because of the limitations in the lithographic resolution of the microfabrication process and the slight discordance between the design layout on the mask and the actual fabricated devices, the final tuning for the design optimization also relies on the DFTM loop. The next section presents the fabrication process, including postprocesses for MUMPs chips thinning, backside polishing, optical tunnel DRIE etching, and antistiction plasma-enhanced chemical-vapor deposition (PECVD) coating.

IV. Fabrication

The prototypes were fabricated in MEMSCAP MUMPs, a Multi-User MEMS Process [40], with a newly developed postprocess (see Fig. 13) and a chip carrier system (see Fig. 14). This system can hold and protect an individual 1 cm^2 MUMPs chip during back side lithography and deep reactive ion etching

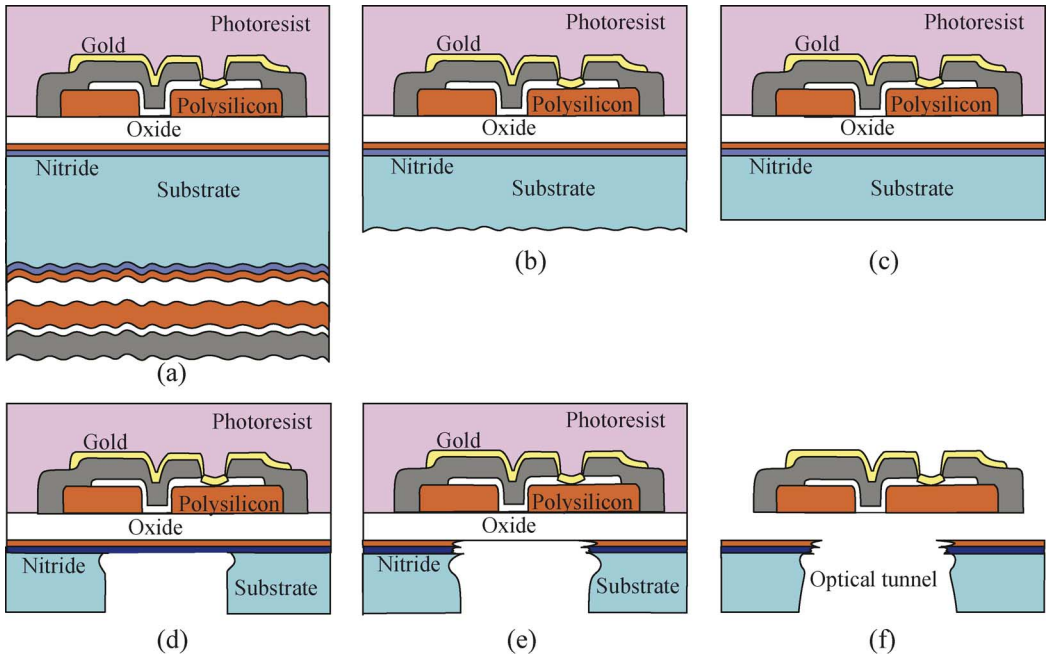

Fig. 13. The process flow chart for fabrication of the optical tunnel. (a) An unreleased chip. (b) After mechanical polishing. (c) After polish etching. (d) DRIE through hole etching. (e) RIE aperture etching. (f) After releasing.

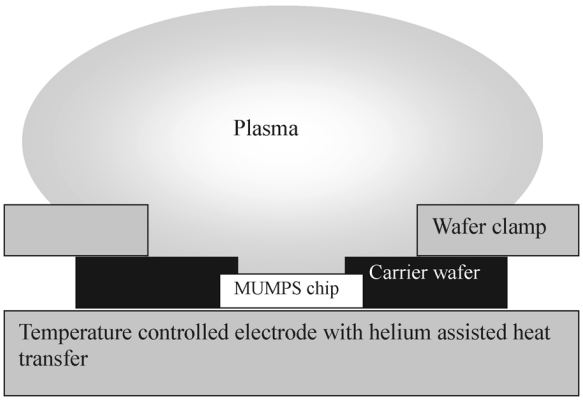

Fig. 14. The chip carrier system can hold the MUMPs chip during the processing in the DRIE chamber under pressurized helium. It is used to provide good heat transfer between the wafer and the chuck electrode.

(DRIE). The purpose of the post-process is to open optical tunnels and adjust apertures to fit various microlens systems. Processing included substrate side mechanical and chemical polishing (chip thinning), double-side-aligned DRIE based optical tunnel etching, aperture adjusting etch with RIE, HF sacrificial oxide removal with supercritical point drying, and C_3F_6 PECVD hydrophobic fluorocarbon polymer coating on MEMSCAP MUMPs chips.

A. Optical Tunnel Postprocessing on MUMPs Chips

To obtain a high contrast transmissive optical switch, an optic tunnel through the opaque silicon substrate should be created exactly under the center of the shutter with accurate alignment. Deep-reactive ion enhanced (DRIE, Oxford Plasmalab 100) etching has been selected to complete this task. Since MUMPs performs most thin film depositions in the LPCVD chamber, the material deposited on the device side of the chip also deposits on the substrate (back) side of the chip. Therefore, it is critical to do a polishing and chip-thinning etch from the substrate side to increase the IR transmission for double-sided alignment before lithography and to ensure the quality of DRIE etching. The unreleased zigzag actuators on the device side of the MUMPs chips are first protected by spinning photoresist AZ4620 and bonding onto a glass carrier with the same photoresist. The MUMPs die is polished mechanically by 600 grade SiC to remove all the LPCVD polysilicon, silicon oxide and silicon nitride layers on the substrate side (the material removal rate is hard to measure precisely on rough and nonhomogeneous surfaces; the average rate is around 1.5 $\mu\mathrm{m/min}$). Then, the chip is removed from the carrier and cleaned with acetone. To protect the material for the polish etchant HNA (HF, nitric acid, and acetic acid 2:15:5) [41], another layer of spin-on photoresist AZ4620 is applied to the device side. After hard baking, the die is covered by melted wax to protect the unreleased actuators from the polish etchant. The wet etching rate of HNA is around 6–7 $\mu\mathrm{m/min}$ at room temperature. After the polish etching is finished, the chip has been thinned to 150 $\mu\mathrm{m}$, and most of the wax is removed with warm water (75 °C). After cooling at room temperature, the photoresist and wax residue on the top of the chip is removed and cleaned with acetone and readied for the substrate side lithography and DRIE through-hole etching (see Fig. 13). The through-hole patterns for optic tunnels are transferred from the photoresist (AZ4620) to the substrate side of the MUMPs chip by an AB-M double-sided IR aligner using one movable objective lens with multi 2 $\mu\mathrm{m}$-alignment marks at corners to achieve accurate alignment (registration accuracy 2–3 $\mu\mathrm{m}$). After developing and drying, the chip is simply inlaid into the carrier system, a 4-inch silicon wafer with a DRIE

through-etched frame. The MUMPs chip rests on a recessed frame over a through-hole that is slightly smaller than the chip. The chip is held and sealed by post-baked photoresist for the DRIE. The chip carrier system (see Fig. 14) was designed and fabricated for MUMPs chips by DRIE to hold the MUMPs chip during the processing under pressurized helium for good heat transfer and temperature uniformity. A stable and uniform temperature between the chip and the chuck electrode is needed to yield uniform etching results. The carrier system also prevents free radicals in the plasma from damaging the polysilicon devices on the device side of the MUMPs chip during the etching.

In DRIE, it is possible to obtain profiles with positive slopes as well as with reentrant profiles by controlling the duration of the etching and deposition (protection) cycles (ratio of etching-time versus deposition-time). A positive profile is desired for the optic channel, but it may decrease the etching rate in DRIE. The thickness variation of the chip can also detrimentally affect the size of the opening. To achieve a good optic tunnel under the shutter, a high aspect ratio Bosch process was selected for the vertical through-hole etching (etching rate is 2.0 $\mu\mathrm{m}/\mathrm{min}$). This etch stops when it reaches the bottom of the nitride layer. The final step of the through-hole etching is accomplished in a Trion Phantom RIE system; SF_6 plasma slowly removes the nitride layer and the Poly0 layer. The Poly0 layer is the endpoint detection layer, once the Poly0 testing structure (here simply a generic Poly0 layer) has been removed, the etching stops at the boundary of the first oxide layer. SF_6 plasma etching also makes the optical channel more positive, which is good for large NA microlenses. After the through-hole etching, a sacrificial oxide removal is performed by immersing the chip in a bath of concentrated HF (49%) at room temperature for 2.5 min, followed by 10 min cleaning in DI water. Liquid CO_2 super-critical point drying (CPD) is used for the MUMPs chip drying to avoid damage due to capillary forces and sticking.

B. Stick Reduction

In order to prevent in-use stiction, besides using critical point release and adding dimples under the structure and bumps for the sidewalls, surface modification with a PECVD hydrophobic fluorocarbon polymer coating [42] has also been applied. The low-surface-energy fluorocarbon film is good for anti-stiction and lubrication. It is deposited in a custom-made chamber under $\mathrm{C}_3\mathrm{F}_6$ plasma at flow rate 2 sccm, pressure 15 0 mtorr, and forward power 20 W. Under these conditions, the deposition rate is around 27 nm/min. After 10 min of deposition, a 274-nm thick (standard deviation 1.5%) carbon-fluorinated polymer has been coated onto the TMOS. The fluorocarbon film is also used as electrical insulator to prevent short circuits between the electrostatic actuator and the electrode. The coating yields a breakdown voltage up to 140 V. After the MUMPs chip is removed from the PECVD chamber, it is ready for testing.

V. Experiments and Discussion

A. Testing Setup

The actuators are tested on a probe station. The probe station is equipped with an A-ZOOM2 laser-ready microscope (3000× magnification) and an internal CCD camera. It is capable of time-resolved testing with a strobe-integrated or a laser-integrated setup (Fig. 15).

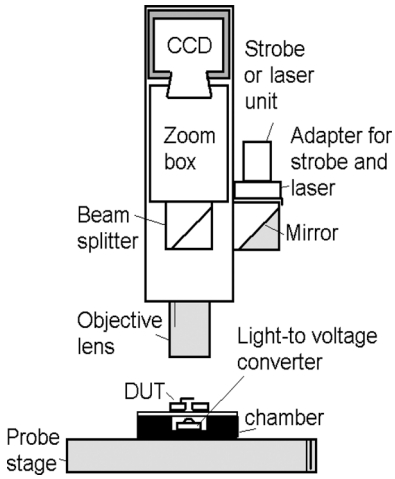

Fig. 15. Test setup with optical microscope, strobe or laser adapter, and device under test (DUT).

Driving signals are electrically contacted to the DUT (device under test) through coaxial cables and microprobes $(\mathrm{tip\ radius} = 0.5\ \mu\mathrm{m})$. An amplifier, MSK103 (M.S. Kennedy Corporation), handles the drive signals from a digital-to-analog PCI high-speed analog output card (National Instruments NI6713, 1 million-samples/s/channel) or a function generator with GPIB interface (Agilent 33120A).

The strobe-based setup, using a pulsed ultrabright 660 nm LED diode (Lumex SSL-LX100133SRC, pulse width 1–10 μs), is capable of independent measurement of displacement at multiple points on the zigzag under periodic motion. The device illuminates only at one specific phase angle of periodic motion and produces a quasi-static image of the zigzag at this specific phase angle.

The laser-integrated test setup incorporates 1) a 50-mW 658-nm laser diode (Hitachi HL6503MG) operated at 2.5 V with a collimating lens, 2) a precision high-speed light-to-voltage converter (TAOS TSL 254) that monitors the amount of light passing through the shutter, 3) an oscilloscope, and 4) a GPIB interface. The laser diode is focused onto the shutters. It works together with the light-to-voltage converter, which has an output pulse rise and fall time around 2 μs with output voltage directly proportional to light intensity (irradiance). Focused laser light passes through the optical channel and illuminates the photo sensor when the shutter is open. The output voltage of the photoconverter can represent the optical tunnel-opening ratio controlled by shutters. The laser-integrated setup allows the monitoring of arbitrary shutter motions in real-time with submicrometer resolution. The detector signal is picked up by an Agilent/Hewlett Packard 54815A Infiniium Oscilloscope.

B. Static Deflection and Side Instability

To measure the static displacement of a zigzag, the magnitude is obtained from a single frame of the video taken with reference

TABLE III
PULL-IN VOLTAGES AND NATURAL FREQUENCIES OF DIFFERENT ZIGZAG DESIGNS. FOUR DESIGNS WERE TESTED IN TWO MUMPS RUNS EACH. VOLTAGE DISPLACEMENT RESULTS ARE SHOWN IN FIG. 17. THESE RESULTS SUGGEST THAT THE NATURAL FREQUENCY MAINLY DEPENDS ON THE WIDTH (I.E., STIFFNESS), WITH STIFFER ZIGZAGS HAVING A HIGHER NATURAL FREQUENCY

MUMPs Run #	44/45	44/45	48/49	48/49
Design	Type1	Type2	Type3	Type4
Zigzag width (μm)	1.5	3.0	1.8	2.0
Zigzag thickness (μm)	1.5	3.5	3.5	3.5
Electrode height (μm)	3.5	3.5	3.5	3.5
Number of teeth	10	10	11	11
Pull-in voltage (V)	38	Not observed	63	Not observed
Measured natural frequency (kHz)	<6.6	38.6	12.6-15.4	16.6-18.6

structures. When the driving voltage supplies a potential difference across the movable zigzag suspension and the fixed electrodes then the electrostatic force moves the shutters according to the applied voltage. Experimentally, a pair of zigzag actuators controls an $18\ \mu\mathrm{m} \times 22\ \mu\mathrm{m}$ opening at 38–114 V with large controllable static displacement, depending on the zigzag geometry and zigzag electrode thickness combination (Table III). Types 2 and 4 provide the zigzag actuator designs with nearly full-range analog tunable capability. The test results show that the zigzag actuator with full-range motion (Type 2) can be operated under analog mode. The pull-in test also shows that the pull-in voltage is very sensitive to the width of the zigzag.

"Pull-in" instability is one of the major concerns for electrostatic actuators, which tends to limit their stable travel range. The unstable behavior is due to the disappearance of the stable balance position of spring force and electrostatic force (a local minimum of the overall potential energy). Usually, for analog switch design, the aim is to avoid pull-in to extend the controllable travel range. For digital switching, the goal is to lower the pull-in voltage for fast switching, low on/off switch power and addressing voltage. Compared to analog switching, digital switch architectures do not require precision servo-control.

Experimentally, the pull-in voltages and stable travel ranges of zigzag actuators depend on the widths of the zigzags. Fig. 16 shows the actuators can controllably travel well beyond the conventional one-third limit of the 11.5 μm full range. Zigzag Type 1 experienced a strong pull-in effect: once pull-in happened, the actuator mechanically stuck to the electrode permanently. Zigzag Type 3 has a long stable travel range and limited pull-in effect (see Fig. 17). Types 2 and 4 have full-range controllable movement. These experimental results show that the zigzag stable driving distance is increased according to its width. This implies one can design a zigzag actuator with controllable stable traveling range simply by manipulating the width of the zigzag, without a complicated layout rearrangement and external circuitry. This is a significant design advantage of the zigzag actuator.

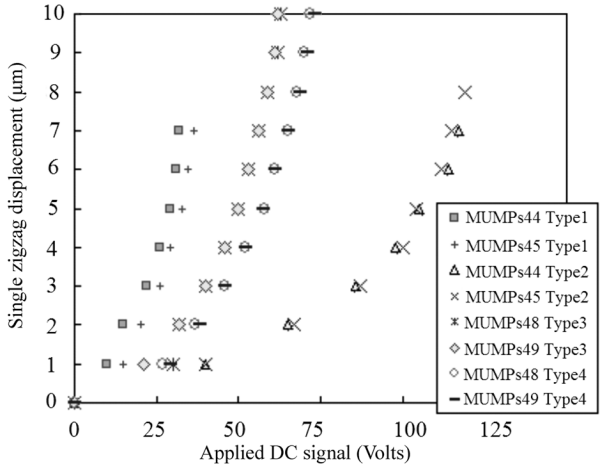

Fig. 16. Experimental results show that the displacement of zigzags before pull-in is proportional to voltage squared and inverse to zigzag area moment of inertia under similar geometric conditions (same number of teeth). Each type of design has been tested on at least two MUMPs runs. It shows good reproducibility of performance.

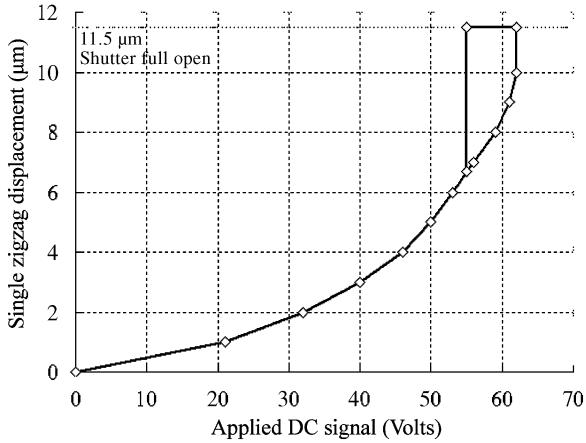

Fig. 17. The hysteresis of zigzag Type 3. Pull-in voltage: 63 V, release voltage: 55 V. Shutter has controllable displacement within 87% of full range of motion.

C. Resonant Frequency

Depending on the width of the zigzag, its measured fundamental frequency varies between 6.6 kHz and 38.6 kHz (Table III). The magnitude of resonance is observed by checking the image blur of a sinusoidally vibrating shutter, which is obtained from a single frame of video under 30 frames/s taken during motion. The blur region denotes the shutter vibration amplitude.

The lithographic resolution used in fabrication, process variations (see Fig. 18) and the geometric discrepancies between design and physical fabricated devices cause these measured fundamental frequencies to be lower than the analytic estimation. Possible reasons are: (1) During pattern transfer from lithographic mask to plasma etched polysilicon structure, we observe some dimension loss on the sidewall of the geometry. Since the width of the microfabricated zigzag is smaller than the designed value, the area moment of inertia decreases, thus making the

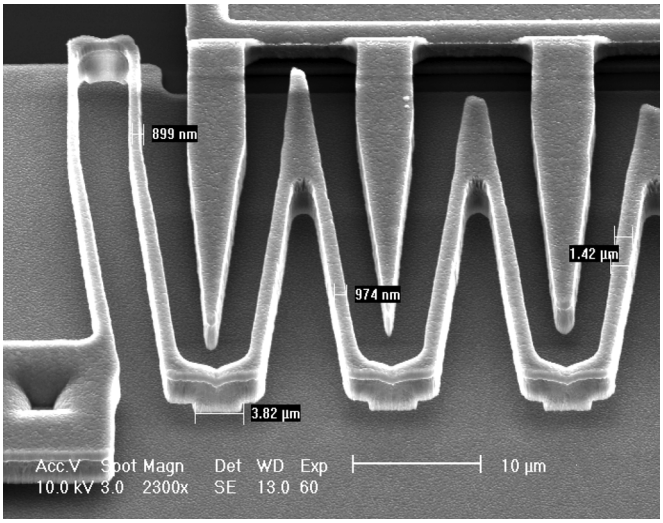

Fig. 18. Discrepancies in beam width of zigzag actuator due to process variation.

fundamental frequency of the microfabricated device smaller than the analytic prediction from the layout. (2) The footing effect caused by reflected ions from the charged oxide surface [43] further decreases the area moment of inertia of the 1.5 to 2.0 μm wide zigzag (see Fig. 19).

D. Settling Time

Settling time is the time required after a step response of the shutters to stop oscillating or ringing and to move into their final position. When the zigzag actuator takes advantage of the pull-in effect, it opens against stoppers in a stable position, thus the shutter can be operated under digital mode. In this case, settling time can be ignored, since the pull-in voltage holds the shutter tightly against the stoppers with negligible ringing.

However, the settling time is critical if the shutter is operated under analog mode. Under this mode, the transmitted light intensity is controlled by the ratio of shutter opening, which is driven by analog signals. The settling time test was accomplished on a Type 2 TMOS in the laser-integrated setup. When a laser beam passes through the optical channel and onto the photo sensor, the light intensity is manipulated by the opening of the shutter and sensed by the photodetector. To measure the settling time under step response, a square-wave signal is used to drive the zigzag actuator. When the step signal jumps from 0 to 100 V, the two shutters yield an 8 μm (67%) optical-channel opening. The shutters open with mechanical ringing until they settle to their final position under system damping. The light intensity is oscillating because of the ringing shutters. This is monitored by a precision high-speed light-to-voltage converter (TAOS TSL 254, sensor rise and fall time is around 2 μs). The sensor output voltage is directly proportional to light intensity. The period of the square-wave is chosen to be longer than the settling time to complete the measurement before the shutters are actuated by the next voltage step in the square wave. The measurement result shows the rise time is around 10 μs; the fall time is around 20 μs. The asymmetry in rise and fall times is caused by the different dominant forces of electrostatic charging and mechanical spring restoring, respectively. The settling time is around 2 ms, as shown in Fig. 20. The thickness, proportional to mass, of the opaque gold layer on shutters also impacts the settling time. If the shutters are not coated with gold, they become lighter and the settling time of TMOS Type 3 is decreased to 1.6 ms, however, they only yield a contrast ratio around 7:1 (measured by the light-to-voltage converter).

In the digital mode, to achieve a single color display module with 256-level intensity scale at 60 frames/s requires digital switching at 15 360 Hz. Then, one on-off switch needs to be completed within 65 μs, which is feasible with a rise and fall time of 10 and 20 μs, respectively. One can integrate three single-color display modules into one full-color projection system, which would be similar to the configuration in 3LCD technology. However, if one wants to take advantage of digital light processing (DLP) technology, the design goal for working frequency should include another factor of 3 for time-sequential color.

In the analog mode, a 60 Hz arbitrary but periodic drive signal is applied to the Type 3 TMOS; this test signal yields five individual and easily distinguishable intensity levels. The driving signal and the corresponding light intensity levels are recorded as shown in Fig. 21. The maximum number of analog gray levels is determined by the ability to accurately control the shutter position. As demonstrated in Figs. 16 and 17, shutter displacement follows a quadratic relationship with applied voltage across a range of tens of volts, providing the capability for high-resolution open-loop control. However, transmissive light intensity can not be expected to be linear in shutter position; an initial experimental calibration between applied voltage and light intensity will be necessary.

Though high frequency light ringing may not be noticeable to the naked eye, to eliminate ringing caused by settling and to achieve a well-defined pixel, the back light would need to be turned off during the shutter's ringing state and turned back on during the shutter's holding state, requiring directly modulated light sources (e.g., LED). If we allow the back light to turn off for 2 ms per frame, then we can obtain a well-defined pixel for about 14.7 ms or 18.0 ms, which is around 88% or 90% of the frame period for PAL (20 ms) or NTSC (16.7 ms) standards, respectively. This optical efficiency is superior to common liquid crystal polarized optical attenuators. A proper preconditioned driving signal exploiting the system dynamics also can reduce ringing and improve the switching time significantly.

E. Reliability and Lifetime

There are over 180 zigzag actuators on each shared MUMPs chip. The postprocess does not physically damage any zigzag actuator. However, understanding the failure modes of the TMOS is critical for the reliability and lifetime assessment of these actuators. They include optical and mechanical failures. Optical failures originate mainly from over-etching or misalignment during through-hole etching. Careful design and a well-controlled process can avoid these failures. Mechanical failures are caused by actuators being stuck because of contamination, levitation, electrode damage and shutter failure during testing. Levitation or out-of-plane movement is due to an asymmetrical electrical field distribution in the vertical direction and tends to let the zigzag "jump" over the stoppers

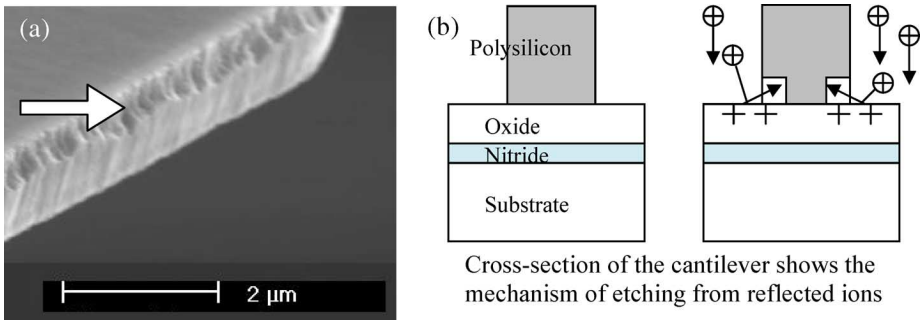

Fig. 19. (a) SEM photograph showing the footing effect at the bottom side of a Poly1 structure. It is caused by etching of ions reflected from the charged oxide surface during the MUMPs Poly1 etch. (b) Cross-section diagram of a cantilever shows the mechanism of etching by reflected ions.

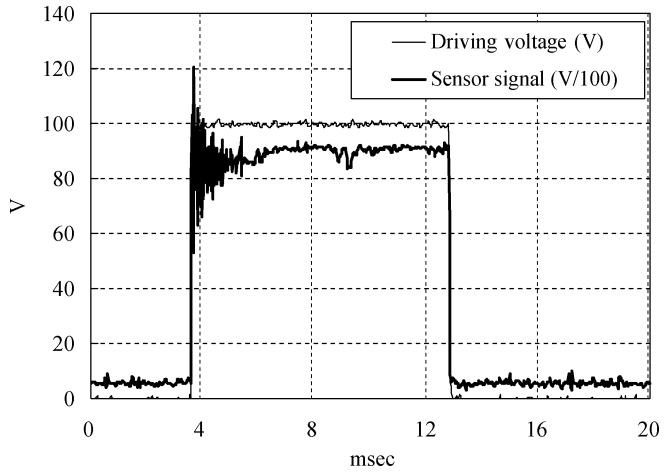

Fig. 20. Shutter settling time (Type 2 zigzag actuator pair with gold on shutters).

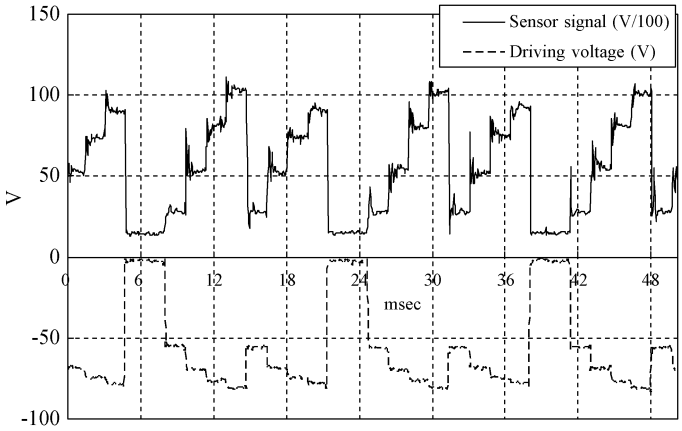

Fig. 21. Light intensity versus 60 Hz arbitrary driving signal (Type 3 zigzag actuator pair without gold on shutters). Voltages between 0 and −80 V (dashed lower curve) and corresponding intensity signals from the photodiode (black upper curve) are shown. Both signals use the same x-axis.

and stick on the electrodes. This problem can be solved by using double height Poly1 and Poly2 as zigzag structural layer in order to increase its vertical stiffness.

Among all the tested designs, Type 1 has the weakest mechanical strength, and the lowest natural frequency; it stuck to the electrode occasionally. Type 2 has the strongest structure; however, it requires the highest driving voltage. Type 3 and Type 4 can be driven with relatively low voltage and yield almost full range controllable movement; they can be applied in a practical TMOS device. Therefore, the fatigue and reliability tests have been performed on Type 3 and Type 4. For a single zigzag Type 3 actuator, after more than 7.6×10^9 cycles under resonance frequency (12.6 kHz, range 15 μm, sinusoidal excitation $V_{\min} = -48$ V, $V_{\max} = 48$ V), no fatigue or frequency shifts have been observed.

For a dual actuator Type 4 TMOS, after more than 1.78×10^9 cycles (2 kHz, full-range digital switching mode), no defects or shutter damage caused by collision were apparent. Shutters actuated for several billion cycles did not show any noticeable mechanical defect such as wear or beam rupture. The contact surface was also investigated and no deterioration has been observed. The precise shutter movement was monitored under the strobe-integrated setup. The bounce caused by shutter collision in the closed state was below the limit for optical observations (less than 1 μm), which is smaller than the overlapping length of the shutters (1.5 μm). We did not observe that shutter-bouncing would cause any shutter engagement within the tested frequency range. However, above the fundamental frequency, a difference in mass between the two shutters would shift the shutter engagement position away from the center of the optical tunnel. A 3×3 array of nine shutters (Type 4) has been successfully actuated except for one failed device due to shutter sticking (yield ratio 88.8%). Their typical resonance frequency is around 18 kHz with an addressing voltage around 75 V.

VI. Conclusion and Summary

The zigzag design conquers the traditional dilemma in microactuators: *using an electrostatic actuator to generate large displacement within a small design space with relatively low voltage*. Zigzag electrostatic actuator designs enhance the force-to-stiffness ratio for large displacement. Theoretical and experimental results demonstrate that the zigzag design has many advantages. First, it can achieve full range of controllable motion for stable analog positioning. This is useful for controlling transmissive light intensity for each pixel in a variety of tuning applications. Second, the stable traveling range (pull-in voltage) can be adjusted simply by manipulating the width of the zigzag without involving complicated layout rearrangements. Thus, zigzag actuators also can be driven under digital switch mode. Third, the space-efficient configuration allows

the zigzags to be arranged into a densely packed array for high-resolution displays or optical data storage systems with low unit cost. Finally, low-drive current can be achieved with low-power consumption.

One can package a limited number of microfabricated TMOS arrays into an individual module, and then assemble these modules into a big wall display. The tightest arrangement, which aligns TMOS units (size $125 \times \sqrt{2} = 176.8\ \mu\mathrm{m}$ by $125/\sqrt{2} = 88.4\ \mu\mathrm{m}$) at a 45-degree angle relative to the pixel array, can achieve an optical tunnel spacing of 125 μm pitch. However, a less compact packing with optical tunnel spacing of 200 μm pitch is recommended for integrating control electronics or spacers onto the device side of the TMOS chip.

Integration of the microlens array and TMOS chip into a complete module is beyond the scope of this paper. A functional TMOS display module should consist of a well-aligned microlens array and anti-electrostatic shield to achieve good optical efficiency and a reliable operating environment. The packaged TMOS module should also have good thermal management and durable structure to prevent device damage from thermal or mechanical stress and unwanted bending.

Low manufacturing cost is crucial for commercialization. In particular, using $12''$ silicon wafers to produce monolithic $12''$ TMOS displays would be prohibitive. Rather, large displays could be achieved by tiling of smaller TMOS modules. Microlens arrays can focus the light for each module through a TMOS that is substantially smaller than the module itself. For further cost reduction, it is also possible to build the surface-micromachined TMOS directly on glass, quartz, or polymer substrates with integrated microlens arrays. Using a transparent substrate would eliminate the need for through-hole etching. Tiling the TMOS modules into a wall display with uniform brightness and hue while avoiding seam artifacts is a significant remaining challenge.

Finally, besides using the TMOS as a display component, this space-efficient device also can be useful for other applications such as optic network attenuators.

ACKNOWLEDGMENT

The authors gratefully acknowledge M. Afromowitz and Y. I. Shen for valuable discussions and suggestions. The authors would like to thank K. Kerkof, K. Nishimura, E. Miller, A. Tombros, G. Holman, and K. Ritala of the Washington Technology Center; D. Qin and G. Golden of the Center for Nanotechnology at the University of Washington; W. Ciridon and B. Ratner of the University of Washington Engineered Biomaterials Center, and W. Walker of Oxford Instruments for their technical training and assistance, and M. Esashi, H. Fujita, and O. Tabata for their hospitality during a sabbatical visit at their laboratories.

REFERENCES

[1] K. Wang, K. F. Böhringer, M. Sinclair, and G. Starkweather, "Highly space-efficient electrostatic zigzag actuator for transmissive micro-optic switches," in *Proc. 12th Int. Conf. Solid-State Sensors and Actuators (Transducers'03)*, Boston, MA, 2003.

[2] T. T. King, G. Kletetschka, M. A. Jah, M. J. Li, M. D. Jhabvala, L. L. Wang, M. A. Beamesderfer, A. S. Kutyrev, R. F. Silverberg, D. Rapchun, D. S. Schwinger, G. M. Voellmer, S. H. Moseley, and L. M. Sparr, "Cryogenic characterization and testing of magnetically actuated microshutter arrays for the James Webb space telescope," in *Proc. Solid-State Sensor and Actuator Workshop*, Hilton Head Island, SC, 2004.

[3] J. Kimmel, J. Hautanen, and T. Levola, "Display technologies for portable communication devices," *Proc. IEEE*, vol. 90, no. 4, pp. 581–586, 2002.

[4] C. W. McLaughlin, "Progress in projection and large-area displays," *Proceedings of the IEEE*, vol. 90, no. 4, pp. 521–532, Apr. 2002.

[5] H. Kawamoto, "The history of liquid-crystal displays," *Proc. IEEE*, vol. 90, no. 4, pp. 460–500, Apr. 2002.

[6] H. Uchiike and T. Hirakawa, "Color plasma displays," *Proceedings of the IEEE*, vol. 90, no. 4, pp. 533–539, 2002.

[7] R. H. Friend, "Organic electroluminescent displays," in *Proc. EuroDisplay*, Berlin, Germany, 1999.

[8] L. J. Hornbeck and W. E. Nelson, "Bistable deformable mirror device," in *OSA Technical Digest Series: Spatial Light Modulators and Applications*, 1988, p. 107.

[9] R. Apte, F. Sandejas, W. Banyai, and D. Bloom, "Grating light valves for high resolution displays," in *Solid State Sensors and Actuators Workshop*, 1994.

[10] S. Bains, "Micromechanical display uses interferometric modulation," SPIE Optical Engineering Reports 2000, vol. 199.

[11] [Online]. Available: http://www.parc.com/research/projects/paperdisplays/2002

[12] A. Biffen, "Understanding HDTV–A Comparison," 2004 [Online]. Available: http://softwareforhomes.com/HDTV-Home-Theatre.htm

[13] H. Urey, "Spot size, depth-of-focus, and diffraction ring intensity formulas for truncated Gaussian beams," *Appl. Opt.*, vol. 43, no. 3, 2004.

[14] R. T. Howe and R. S. Muller, "Resonant-microbridge vapor sensor," *IEEE Trans. Electron Devices*, vol. ED-33, pp. 499–506, 1986.

[15] M. A. Schmidt and R. T. Howe, "Resonant microsensors," in *Tech. Dig., 4th Int. Conf. Solid-State Sensor and Actuators*, Tokyo, Japan, 1987.

[16] W. Newell, "Novel circuit aspects of the resonant gate transistor," in *Proc. IEEE Int. Solid-State Circuits Conf.*, 1966.

[17] P. B. Chu and K. S. J. Pister, "Analysis of closed-loop control of parallel-plate electrostatic microgrippers," in *Proc. IEEE Conf. Robot. Automat.*, San Diego, CA, 1995.

[18] J. I. Seeger and S. B. Crary, "Stabilization of electrostatically actuated mechanical devices," in *Proc. Transducers'97*, Chicago, IL, 1997.

[19] E. K. Chan and R. W. Dutton, "Electrostatic micromechanical actuator with extended range of travel," *J. Microelectromech. Syst.*, vol. 9, no. 3, pp. 321–328, 2000.

[20] E. S. Hung and S. D. Senturia, "Leveraged bending for full-gap positioning with electrostatic actuation," in *Proc. Solid-State Sensor and Actuator Workshop*, Hilton Head, SC, 1998.

[21] R. Legtenberg, J. Gilbert, S. D. Senturia, and M. Elwenspoek, "Electrostatic curved electrode actuators," *J. Microelectromech. Syst.*, vol. 6, no. 3, pp. 257–265, 1997.

[22] G. Perregaux, S. Gonseth, P. Debergh, J. P. Thiebaud, and H. Vuilliomenet, "Arrays of addressable high-speed optical microshutters," *J. Microelectromech. Syst.*, vol. 10, 2001.

[23] R. Legtenberg, A. W. Groeneveld, and M. Elwenspoek, "Comb-drive actuators for large displacements," *J. Micromech. Microeng.*, vol. 3, pp. 320–329, 1996.

[24] M. Mita, M. Arai, S. Tensaka, D. Kobayashi, and H. Fujita, "A micromachined impact microactuator driven by electrostatic force," *J. Microelectromech. Syst.*, vol. 12, no. 1, pp. 37–41, 2003.

[25] M. S. Rodgers, S. Kota, J. Hetrick, Z. Liz, B. D. Jensen, T. W. Krygowskil, S. L. Miller, S. M. Barnes, and M. S. Burg, "A new class of high force, low-voltage, compliant actuation systems," in *Proc. Solid-State Sensor and Actuator Workshop*, Hilton Head Island, SC, 2000.

[26] R. R. A. Syms, B. M. Hardcastle, and R. A. Lawes, "Bulk micromachined silicon comb-drive electrostatic actuators with diode isolation," *Sens. Actuators A: Phys.*, vol. 63, no. 1, pp. 61–67, 1997.

[27] J. T. Nee, K. Y. Lau, and R. S. Muller, "A flat high-frequency scanning micromirror," in *Proc. Solid-State Sensor and Actuator Workshop*, Hilton Head Island, SC, 2000.

[28] J.-L. A. Yeh, H. Jiang, and N. C. Tien, "Integrated polysilicon and DRIE bulk silicon micromachining for an electrostatic torsional actuator," *J. Microelectromech. Syst.*, vol. 8, no. 4, pp. 456–465, 1999.

[29] T. Hirano, T. Furuhata, K. J. Gabriel, and H. Fujita, "Design, fabrication, and operation of submicron gap comb-drive microactuators," *J. Microelectromech. Syst.*, vol. 1, no. 1, pp. 52–59, 1992.
[30] M. A. Rosa, S. Dimitrijev, and H. B. Harrison, "Improved operation of microelectromechanical comb-drive actuators through the use of a new angled comb finger design," in *Proc. SPIE Conf. Smart Materials, Structures, and MEMS*, 1997.
[31] W. Ye, S. Mukherjee, and N. C. MacDonald, "Optimal shape design of an electrostatic comb drive in microelectromechanical systems," *J. Microelectromech. Syst.*, vol. 7, no. 1, pp. 16–26, 1998.
[32] W. Ye and S. Mukherjee, "Design and fabrication of an electrostatic variable gap comb drive in micro-electro-mechanical systems," *Proc. ASME Micro-Electro-Mechanical Systems (MEMS)*, vol. 66, pp. 537–544, 1998.
[33] B. D. Jensen, S. Mutlu, S. Miller, K. Kurabayashi, and J. J. Allen, "Shaped comb fingers for tailored electromechanical restoring force," *J. Microelectromech. Syst.*, vol. 12, no. 3, pp. 373–383, 2003.
[34] A. L. Pisano and Y. H. Cho, "Mechanical design issues in laterally-driven microstructures," in *Proc. Transducers'89*, Montreux, Switzerland, 1989.
[35] W. C. Tang, T. H. Nguyen, and R. T. Howe, "Laterally driven polysilicon resonant microstructures," *Sens. Actuators A: Phys.*, vol. A 20, pp. 25–32, 1989.
[36] J. Grade, H. Jerman, and T. Kenny, "Design of large deflection electrostatic actuator," *J. Microelectromech. Syst.*, vol. 12, no. 3, pp. 335–343, 2003.
[37] J. M. Gere and S. P. Timoshenko*, Mechanics of Materials*, 3rd ed. Boston, MA: PWS-Kent, 1990.
[38] C. F. Beards*, Structural Vibration Analysis and Damping*. Oxford, U.K.: Butterworth-Heinemann, 1996, p. 105C. F. Beards, Structural Vibration Analysis and Damping 1996, p. 105.
[39] [Online]. Available: http://www.ansoft.com
[40] D. A. Koester, R. Mahadevan, H. B. , and K. W. Markus*, MUMPs Design Handbook*. Milpitas, CA: JDS Uniphase, 2001.
[41] B. Schwartz and H. Robbins, "Chemical etching of silicon, IV. Etching technology," *J. Electrochem. Soc.*, vol. 123, no. 12, pp. 1903–1909, 1976.
[42] R. d'Agostino, Ed.*, Plasma Deposition, Treatment, and Etching of Polymers*. Boston, MA: Academic, 1990.
[43] A. A. Ayon, S. Nagle, L. Frechette, A. Epstein, and M. A. Schmidt, "Tailoring etch directionality in a deep reactive ion etching tool," *J. Vac. Sci. Technol.*, vol. B18, no. 3, pp. 1412–1416, 2000.

Kerwin Wang received the B.S. degree in mechanical engineering from Chung Yuan Christian University, Taiwan, the M.S. degree in mechanical engineering from the State University of New York at Buffalo, NY, and the Ph.D. degree in electrical engineering from the University of Washington, Seattle, in 2004.

During his dissertation work on micro-display modules, he invented, modeled, and tested zigzag actuators and floating sliders; he also held an internship from Microsoft Research, Redmond, WA. Upon completion of his Ph.D. degree, he spent a year as a Postdoctoral Researcher at the University of Washington, where he investigated micro/nanoassembly techniques. In July 2005, he was hired as a Visiting Postdoctoral Researcher at the Intel Component Research Group and developed high-packing-density micro-assembly for solid-state cooling applications.

Michael Sinclair received the undergraduate and graduate degrees in electrical engineering from the Georgia Institute of Technology (Georgia Tech), Atlanta.

He worked for a while for Western Electric and then joined the research team at Georgia Tech. There, except for a brief interlude to help start and grow a flight simulation company, he has worked in many aspects of hardware research including radar, optics, high-powered lasers, data acquisition, missile simulation, bioelectronics, surgical simulation, telemedicine, and robotics. He was Director of the Multimedia Research Lab that was instrumental in helping Atlanta win the right to host the 1996 Olympics. He joined Microsoft's Research group in 1998 as a Sr. Researcher. One of his recent interests at Microsoft is in the field of MEMS (microelectromechanical systems) as a possible solution to a number of interface problems.

Gary K. Starkweather received the B.S. degree in physics from Michigan State University, East Lansing, in 1960 and the Master's degree in optics from the University of Rochester, Rochester, NY, in 1966.

He has spent over 40 years in the imaging sciences and holds over 44 patents in the fields of imaging, color, and hardcopy devices. From 1962 to 1964, he worked for Bausch & Lomb, Inc., Rochester. From 1964 until 1988, he was employed by Xerox Corporation, where he became a Senior Research Fellow. While at the Xerox Palo Alto Research Center, or PARC, he invented the laser printer. From 1988 until 1997, he was employed by Apple Computer as an Apple Fellow involved in Publishing and Color Imaging products and research. He is part of Microsoft Research as an Architect working on displays and information processing. He has published many papers and has written a book chapter entitled, "High Speed Laser Printers" (New York: Academic). He continues to serve on several technical committees involved in display and color-related imaging issues. He has lectured at both Stanford University and UCLA.

Mr. Starkweather has received a number of awards for this work, including the Xerox President's Achievement Award (1977), the Johann Gutenberg Prize from the Society for Information Display (1987), and the David Richardson medal from the Optical Society of America (1991). In 1994, he received a Technology Academy Award for his consulting work with Lucasfilm and Pixar on color film scanning. In 2002, he was inducted into the Technology Hall of Fame at COMDEX.

Karl F. Böhringer (S'94–M'97–SM'03) received the Dipl.-Inform. degree from the University of Karlsruhe, Germany, in 1990 and the M.S. and Ph.D. degrees in computer science from Cornell University, Ithaca, NY, in 1993 and 1997, respectively.

From 1994 to 1995, he was a Visiting Scholar at Stanford University, Stanford, CA, and from 1996 to 1998, he was a Postdoctoral Researcher at the University of California, Berkeley. He joined the Electrical Engineering Department at the University of Washington in Seattle, WA, in 1998, where he currently Associate Professor. He also held visiting faculty positions at the Universities of Tohoku, Tokyo, Kyoto, Japan, and São Paulo, Brazil. His research interests include microelectromechanical systems (MEMS), manipulation and assembly from macro- to nanoscales, microfluidic systems for the life sciences, and microrobotics. He has created, among others, multibatch self-assembling systems, massively parallel microactuator arrays, and a walking microrobot.

Dr. Böhringer is a member of the Society for Nanoscale Science, Computing and Engineering (ISNSCE), the American Society for Information Sciences (GI). He was awarded a Long-Term Invitational Fellowship for Research in Japan by the Japan Society for the Promotion of Science (JSPS) in 2004, an IEEE Robotics and Automation Society Academic Early Career Award in 2004, an NSF CAREER Award in 1999, and an NSF Postdoctoral Associateship in 1997. His work was listed among the "Top 10 Science Stories of 2002" in *Discover* magazine. He is an Associate Editor for the IEEE/ASME JOURNAL OF MICROELECTROMECHANICAL SYSTEMS and the IEEE TRANSACTIONS ON AUTOMATION SCIENCE AND ENGINEERING, and has served, among others, on technical program committees for IEEE MEMS and Transducers conferences.